Space Sci Rev (2010) 153: 249–271
DOI 10.1007/s11214-010-9642-2

Radar Signal Propagation and Detection Through Ice

Wlodek Kofman · Roberto Orosei · Elena Pettinelli

Received: 1 September 2009 / Accepted: 1 March 2010 / Published online: 31 March 2010

Abstract In this paper we describe the existing and planned radar measurements of the planetary bodies. The dielectric properties of water ice and other potential surface and subsurface materials are discussed, as well as their dependency on temperature and structure. We then evaluate the performance of subsurface sounding radars using these parameters. Finally we describe some laboratory technique to help interpret the radar data, presenting some results obtained using dielectric spectroscopy methods.

Keywords Dielectric properties · Radar · Laboratory measurements

1 Introduction—What Can Be Learned from Radar Observations?

Radio-echo sounding (RES), or ice-penetrating radar, is a well established geophysical technique, similar to ground-penetrating radar, which has been employed for more than five decades to investigate the structure of ice sheets and glaciers in Antarctica, Greenland, and the Arctic. It is based on the transmission of radar pulses at frequencies in the MF, HF and VHF portions of the electromagnetic spectrum into the surface to detect reflected signals from subsurface structures (see e.g. Bogorodsky et al. 1985).

Ground-penetrating radar is particularly effective on glaciers because ice is the most transparent natural material in this range of frequencies. The ice-covered Lake Vostok in

W. Kofman (✉)
Laboratoire de Planetologie de Grenoble, CNRS/UJF, BP 53, 38041 Grenoble, France
e-mail: wlodek.kofman@obs.ujf-grenoble.fr

R. Orosei
Istituto Nazionale di Astrofisica, Istituto di Fisica dello Spazio Interplanetario,
Via del Fosso del Cavaliere, 100, 00133 Roma, Italy

E. Pettinelli
Dipartimento di Fisica "E. Amaldi", Università Roma Tre, Via della Vasca Navale 84,
00146 Roma, Italy

Antarctica was characterized through more than 4 km of polar ice. Cold ice is more transparent than warm ice, so that it is expected that at the temperatures of the outer Solar System this technique could provide detection of much deeper subsurface structures (Blankenship et al. 2010).

An electromagnetic wave propagating through a medium is attenuated, scattered and dispersed. Its distortion depends on the dielectric characteristics of the medium and its homogeneity at the wavelength scale. The electromagnetic pulse emitted from orbiting ice-penetrating radar would be subject to scattering from the irregular natural surface of an icy moon, and it would be scattered by volume inhomogeneities and attenuated in the dielectric subsurface medium before reaching any subsurface dielectric discontinuity causing a reflection.

The capability of subsurface sounding radar to detect an underground dielectric discontinuity is thus strongly dependent on the medium through which the radar pulse propagates. For icy bodies the physical properties of water ice and the effect of impurities in the ice play a major role.

Radar sounding is the only remote sensing technique allowing the study of the subsurface of a planet from orbit. By detecting dielectric discontinuities associated with compositional and/or structural discontinuities, it is possible to map the stratigraphy, i.e. the distribution characteristics of ice and/or rocks vs. depth, which can be of fundamental importance to better understand the dynamics and the history of the first meters to kilometers of the subsurface (depending on frequency and dielectric properties of the material). On the other hand, the estimation of the propagation time and the signal attenuation, also allows us to retrieve some information on the subsurface petrophysical properties like density and material composition. Moreover, the form of the received signal gives some information about the surface and the volume scattering, from which the size distribution of inhomogeneities can be inferred. All this nonwithstanding, the information obtained with subsurface sounding radars should be compared and integrated with other observations (infrared, visible or in situ analysis) to interpret inferred petrophysical properties in an unambiguous way.

In this chapter we describe the existing and planned radar measurements of the planetary bodies. The dielectric properties of water ice and other potential surface and subsurface materials are discussed, as well as their dependency on temperature and structure. We then evaluate the performance of subsurface sounding radars using these parameters. Finally we describe some laboratory technique to help interpret the radar data, presenting some results obtained using dielectric spectroscopy methods.

2 Overview of Radar Observations of Icy Satellites

Radar observations of the icy satellites were obtained from the Earth using the Goldstone and Arecibo radar (Ostro et al. 1992). The measurements of the reflected signal by the surface and subsurface of Galilean satellites and of Saturn's icy satellites were made in the 3.5–70 cm wavelength range. Recently also observations of the Saturn's satellites were made using Cassini 2.2 cm radar. The Arecibo and Goldstone measurements used essentially transmitted circularly polarized and, rarely, linearly polarized signals. The reception of returning signal was in the same circular (SC) (or same linear SL) and opposite circular (OC) (orthogonal linear OL) polarizations. The radar target's properties are measured by its albedo that is defined by the radar cross section divided by the projected area of the observed surface. The total radar albedo is $\mathrm{TP} = \mathrm{SL} + \mathrm{OL} = \mathrm{SC} + \mathrm{OC}$ and the polarization ratio is $\mu_c = \mathrm{SC}/\mathrm{OC}$ (OL/SL). For a polished metal sphere of the radius of the observed bodies the

single back reflections would be entirely OC (or SL) and the polarization ratios equal zero. In this case the radar albedo would equal the surface's Fresnel coefficient.

The reflections from rough surfaces (or produced by multiple reflections or refractions) produce power on two polarizations. For instance, for randomly oriented dipoles, $SC/OC = 1$ and $OL/SL = 1/3$. The echoes from Earth-like planets are characterised by the quasi specular reflection having $SC/OC \cong 0.3$ due to the much stronger direct reflection compared to the power scattered by the surface and subsurface. The total albedo for Earth-like planets or for asteroids are of the order of $TP \sim 0.1$. Figure 1 (Black et al. 2007) summarizes the measurements of total radar albedo and of polarization ratio obtained during the last three decades for icy satellites. One can see that the results are really different from that obtained for the rocky bodies. The polarization ratio is larger than 1 and the total albedo are between 0.3 and 2.6. The total albedo value larger than 1 means that the back reflection is stronger than the reflection from the perfect metal sphere with the same radius as observed body! What is the process responsible for this anomalous high albedo and polarization ratio? The models proposed in the geometrical optics limit included: buried craters effect on the refracted signal (Eshleman 1986), another refraction scattering from subsurface lenses (Hagfors et al. 1997) and volume multiple scattering due to the scatterers embedded in the ice (Hapke 1990). The models were improved (Baron et al. 2003) and the present agreement is that this "anomalous" behaviour results from the multiple scattering within a random medium whose intrinsic microwave absorption is very low. The regoliths of the planetary bodies are very heterogeneous and that combined with the radio transparency of icy regoliths gives the observed radar behaviour. Measurements of radar properties and any inter-satellite variations address issues of surface characteristics and formation histories.

The unusual radar properties of icy satellite surfaces are thus determined by a combination of the structure of the regolith, providing many dielectric discontinuities by which an incident wave is reflected, and its composition, a transparent material that allows several internal reflections of the same wave without attenuating it significantly.

Subsurface sounding radars operate at much lower frequencies, and electromagnetic propagation at wavelengths of tens of meters is probably unaffected by the small-scale structure of the regolith producing the anomalous reflection observed at cm wavelengths. However, the fact that the surface material is so transparent to electromagnetic waves testifies to a mostly icy composition with a small content of impurities, a very favorable scenario for radar sounding experiments.

3 Interpretation of Radar Measurements

Subsurface radar sounding is now an established technique in planetary exploration, with an history of success (see Phillips et al. 1973; Picardi et al. 2004; Seu et al. 2007a; Ono et al. 2009) and a promising future (e.g. Lebreton et al. 2009). The Consert tomographic radar (Kofman et al. 1998, 2007), the next application of this technique, is on the way to its cometary target on the Rosetta mission. However, radar data have features that depend on instrument characteristics and on the environment in which observations take place, which have to be taken into account for a correct interpretation.

The main parameters determining the performance of an orbiting subsurface sounding radar are frequency and bandwidth of the transmitted pulse. Frequency determines the penetration capability of the radar, while bandwidth controls resolution.

For a wide range of frequencies ranging from MHz to GHz and beyond, dielectric losses (loss tangent) in most natural materials are independent of frequency, so that the number

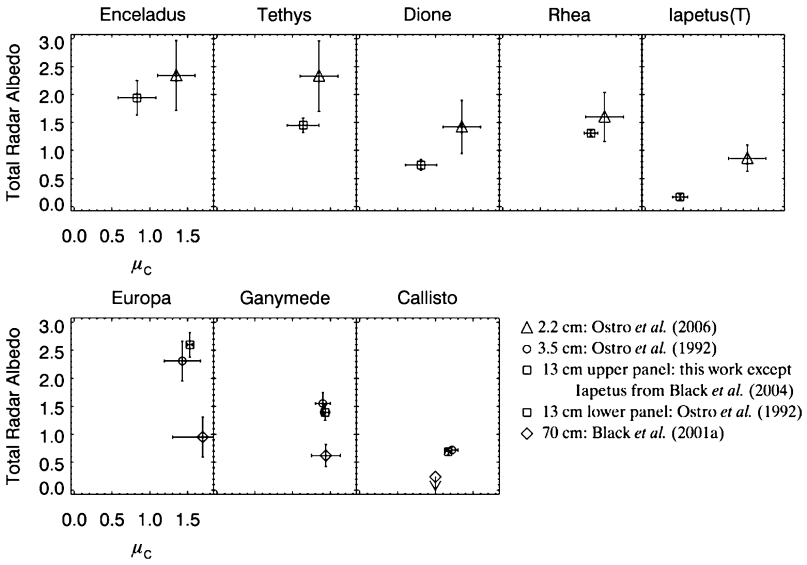

Fig. 1 Plots of total albedo versus circular polarization ratio for each target. Panels with data for Iapetus' trailing (icy) hemisphere and for the icy Galileam satellites are included for comparison. Each point includes data from all available longitudes except Iapetus. The abscissa of each panel is the same as the first panel's. Saturn satellite data at 13 cm wavelength are plotted with the quadrature sum of statistical uncertainties and a 25% systematic uncertainty. At 2.2 cm wavelength the error bars further include assumptions in the ranges of polarization ratios (see text and Ostro et al. 2006). Error bars for the Galilean satellites are the larger of the statistical uncertainties or the range of any variation with longitude. Figure taken from Black et al. (2007)

of wavelengths that an electromagnetic wave can penetrate into the material before being attenuated to a given fraction of its initial amplitude is approximately the same regardless of frequency. This implies that the longer the wavelength, the deeper the radar signal can penetrate before being attenuated below the detection capabilities of the radar. Thus, deep penetration requires that the radar operates at the lowest possible frequency.

In most orbiting radar, the transmitted waveform is a chirp, a long pulse that is linearly modulated in frequency. Chirps are used when the length of the pulse for the desired range resolution is so short that to achieve good signal-to-noise ratio the pulse would require a peak power exceeding the limits imposed by the mission design. The chirp allows a resolution that depends on the bandwidth of the pulse rather than on its duration, but requires processing of the received signal: with a bandwidth B, the approximate time resolution of the output pulse, after processing, is $1/B$. This translates in a vertical resolution of the radar Δr equal to

$$\Delta r = c/(2B\varepsilon^{1/2}) \tag{1}$$

where ε is the relative dielectric permittivity of the material through which the pulse propagates.

Because the bandwidth of the chirp can be at most equal to the highest frequency of the radar pulse (although for practical purposes this limit is never reached), it can be seen that vertical resolution requires the radar to operate at high frequency. Thus, penetration and resolution are conflicting requirements, and no orbiting subsurface sounding radar can achieve one without compromising on the other.

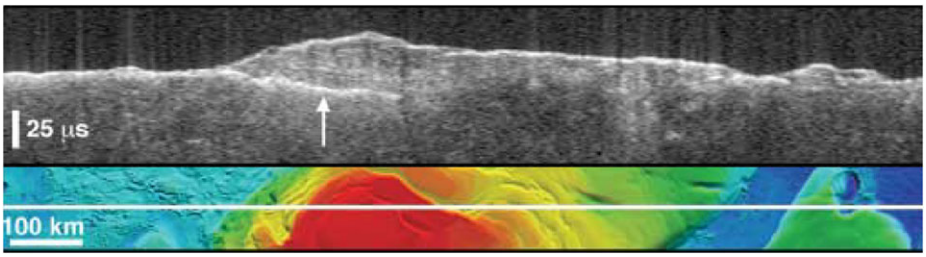

Fig. 2 (*Top*) MARSIS radargram for orbit 2682 above Planum Australe, Mars, showing a bright basal reflector (*arrow*) beneath the ice-rich South Polar Layered Deposits (SPLD). The vertical dimension is round-trip travel time. The apparent curvature of the reflector is an artefact of the time representation of the data. The maximum depth at which the basal reflector could be detected, converting travel time for propagation through water ice, is about 3.5 km. (*Bottom*) Ground track of the spacecraft during data acquisition, shown on a shaded relief topographic map of the south polar region of Mars (adapted from Plaut et al. 2007)

An example of this trade off is the design of the two radars currently operating at Mars, MARSIS (Picardi et al. 2004) and SHARAD (Seu et al. 2007a). They are both synthetic-aperture, orbital sounding radars, carried respectively by ESA's Mars Express and NASA's Mars Reconnaissance Orbiter. MARSIS is capable of transmitting at four different bands between 1.3 MHz and 5.5 MHz, with a 1 MHz bandwidth. SHARAD operates at a central frequency of 20 MHz transmitting a 10 MHz bandwidth. Whereas MARSIS is optimized for deep penetration, having detected echoes down to a depth of 3.7 km over the South Polar Layered Deposits (Plaut et al. 2007), SHARAD is capable of a tenfold-finer vertical resolution, namely 15 m or less, depending on the dielectric constant of the material being sounded (e.g. Seu et al. 2007b).

The difference in the performance of the two radars can be perhaps better appreciated through the examination of Figs. 2 and 3. Both figures show radargrams that are representations of radar echoes acquired continuously during the movement of the spacecraft as grey-scale images, in which the horizontal dimension is distance along the ground track, the vertical dimension is the round trip time of the echo (Fig. 2) or depth (Fig. 3), and the brightness of the pixel is a function of the strength of the echo.

The capability of MARSIS for deep penetration at the expense of vertical resolution can be seen in the radargram in Fig. 2, in which subsurface echoes almost as bright as surface ones are detected down to depths of 3.5 km, but only very faint details of the stratigraphy can be discerned. The minimal attenuation of subsurface reflections—evident through the very weak change of the basal echo brightness with depth—allows one to infer that MARSIS would be able to discern the base of the South Polar Layered Deposits of Mars through at least three or four times their actual thickness.

In Fig. 3 the tenfold-greater vertical resolution of SHARAD, achieved at the expense of penetration, is made evident by the richness of details discernible in the subsurface stratigraphy. The North Polar Layered Deposits of Mars contain much less impurity than the SPLD, and are much more transparent to the radar signal. SHARAD is thus able to see the base of the NPLD and also part of the Basal Unit through almost 1500 m of material, whereas penetration in the SPLD has been found to be approximately half this amount (Seu et al. 2007b).

Subsurface sounding radar data are affected by a number of artifacts that can make it problematic to correctly interpret echoes as either surface or subsurface reflections.

Because of the long (10–100 m) wavelength of radar pulses required in subsurface sounding, it is extremely challenging to produce an antenna that has both an acceptable gain and

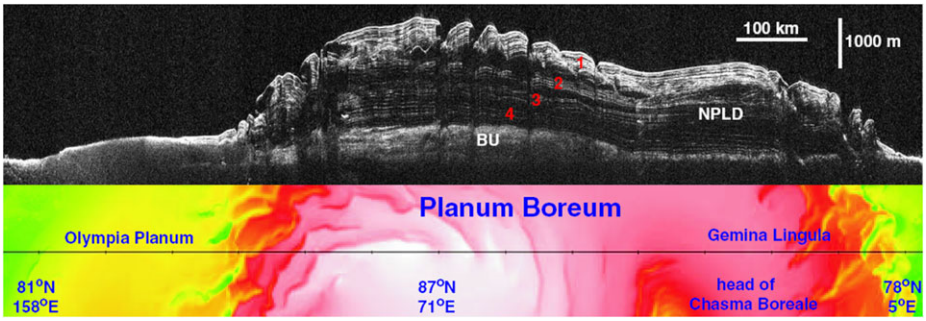

Fig. 3 (*Top*) Radargram from SHARAD orbit 5192 above Planum Boreum, Mars. Range time delay, the usual ordinate in a radargram, has been converted to depth by assigning real permittivities of 1 (corresponding to vacuum) and 3 (water ice) above and below the detected ground surface, respectively. The North Polar Layered Deposit geological unit (NPLD) and the Basal Unit (BU) beneath the NPLD are labelled. Internal radar reflections arise from boundaries between layers differing in their fractions of ice, dust, and sand. The radar reflections in Planum Boreum are clustered into distinct packets of reflectors (numbered). (*Bottom*) Ground track of orbit 5192 shown on a topographic map of the north polar region of Mars (adapted from Phillips et al. 2008)

good directivity. Both MARSIS and SHARAD in fact transmit through dipoles, which have negligible directivity, with the consequence that the radar pulse illuminates the entire surface beneath the spacecraft and not only the near-nadir portion from which subsurface echoes are expected. The electromagnetic wave can then be scattered by any roughness of the surface. If the surface of the body being sounded is not smooth at the wavelength scale, i.e. if the r.m.s. of topographic heights is greater than a fraction of the wavelength, then part of the incident radiation will be scattered in directions different from the specular one. This means that areas of the surface that are not directly beneath the radar can scatter part of the incident radiation back towards it, and thus produce surface echoes that will reach the radar after the echo coming from nadir, which can mask, or be mistaken for, subsurface echoes. This surface backscattering from off-nadir directions is called "clutter". Clutter can produce in a radargram the impression of subsurface structures where there are in fact none. An example is shown in Fig. 4, in which a radargram is compared with a simulated surface echo. What appears in the data to be volume scattering from sediments filling a crater is revealed by simulations to be in fact surface scattering from a crater floor that is flat from the topographic point of view, but must possess a relatively high roughness at meter scale. For data shown in Fig. 4, the effect of roughness below the resolution of the Mars Orbiting Laser Altimeter (MOLA) dataset has been simulated through the use of an analytical formula for the scattering from a random rough surface, but other methods are possible, such as interpolation.

Numerical electromagnetic models of surface scattering, such as those by Nouvel et al. (2004) or Russo et al. (2008), have been routinely used to validate the detection of subsurface interfaces in radargrams. To be effective, however, such models require a knowledge of the topography of the observed surface at scales that are comparable or, better still, much smaller than the wavelength. For example, the MOLA Martian topographic dataset (Smith et al. 2001) has a resolution at the equator of less than 500 m, which is adequate for the MARSIS wavelength range (50–100 m) but requires approximations or interpolations at SHARAD wavelengths (around 15 m).

The presence of a dispersive medium, such as a plasma, between the radar and its observation target can cause a distortion (dispersion) of the transmitted waveform. Such is the

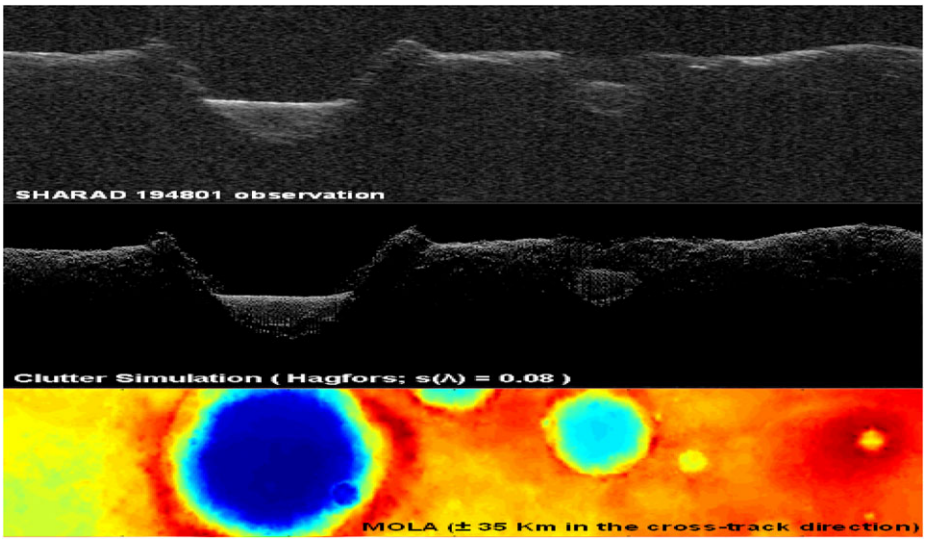

Fig. 4 (*Top*) Radargram from SHARAD orbit 1948 over Meridiani Planum, in which a diffuse echo past the first bright surface echo is visible in flat crater floors, giving the impression that sediments filling the craters are penetrated down to the bedrock. (*Middle*) Simulated radargram obtained through a numerical electromagnetic model of surface scattering making use of the MOLA (Smith et al. 2001) topographic dataset. (*Bottom*) Topographic map centered along the ground track of the MRO spacecraft during observation. It can be recognized that the diffuse echoes seen both in the radargram and in the simulated data originate from the topographically flat yet rough crater floor (adapted from Russo et al. 2008)

case for Mars, which is surrounded by an atmosphere whose upper layers become ionized and excited through solar radiation, producing an ionosphere. As noted above, almost all planetary radar experiments transmit a long chirp to achieve a high signal-to-noise ratio in spite of the usually low power available, with processing on ground required to achieve range resolution. From the mathematical point of view, this processing consists in the correlation of the received signal with the transmitted chirp, and it fails if the phase of the chirp is altered as it propagates to and from the surface. To overcome this problem, several different methods have been proposed, as in Safaeinili et al. (2003), Ilyushin and Kunitsyn (2004), Mouginot et al. (2008), Picardi et al. (2008) and Zhang et al. (2009). This phenomenon should not be encountered by radar sounders exploring the icy moons of the giant planets, however, as most of them (with the notable exception of Titan) are surrounded only by an extremely tenuous exosphere.

In passing, we note that a more serious reason of concern for the performance of a radar sounder for the icy moons of the Solar System is the noise introduced by the giant planets' radio emission at decametric and hectometric wavelengths, especially Jupiter's (see e.g. Zarka et al. 2004). However, the radio noise from Jupiter should not impact the radar performance on the anti-Jovian side of a moon.

A final effect that needs to be taken into account in the geological interpretation of radargrams is the distortion of subsurface interface shapes and slopes caused by the change of the electromagnetic wave propagation velocity in a medium with a relative dielectric permittivity ε greater than that of vacuum. Propagation velocity scales with the inverse of the square root of ε, and is thus lower in a medium with $\varepsilon > 1$, causing a delay in the return from any subsurface reflection with respect to a reflection at the same distance in vacuum. Visually, this results in an apparent "sagging" of subsurface interfaces such as in Fig. 2,

in which the basal echo beneath the SPLD (pointed by an arrow) is in reality at the same level of the topography surrounding the SPLD, but appears to be sloping because of the increasing thickness of the SPLD through which the radar signal propagates. When the value of ε can be derived through other means, it is possible to correct this distortion, such as in Fig. 3, where the dielectric constant of ice ($\varepsilon \approx 3$) has been assumed for the NPLD.

4 Radar Signal Propagation and Detection Through Ice

4.1 Dielectric Properties of Ice

The permittivity ε of a material is a property describing how much more energy is stored through charge separation than in a vacuum. Charges of opposite signs move in opposite directions in response to an external field so that the resultant internal field between the charges opposes the external field. When the external field is removed, the energy stored in this internal field decays as the charges revert back to their original positions. Frequency dependence of permittivity occurs because charge separation does not happen instantaneously.

Charges separate with finite velocities, thus if the external field is reversing polarity too quickly the charges cannot move fast enough to keep up. The frequency at which the charges fully separate and are in constant motion is called the relaxation frequency. At frequencies below the relaxation frequency the permittivity plateaus at the low frequency, or static, limit ε_s, and is often call dielectric constant. At high frequencies above the relaxation frequency the permittivity plateaus at the high frequency limit ε_∞.

The response of the ice crystal is the conduction and the polarization. The polarization will develop in time with some delay which duration depends on temperature. The temperature dependency is described by the Arrhenius function of the form of $\exp(E/kT)$ where E is the activation energy (enthalpy) of the formation process, k the Boltzmann's constant and T temperature.

The classical Debye model takes into account this dependency and the dielectric constant is described by the following equations:

$$\varepsilon = \varepsilon_\infty + \Delta\varepsilon \frac{\Delta\varepsilon}{1 + j\omega\tau}, \quad \omega = 2\pi f \text{ and } \Delta\varepsilon = \varepsilon_s - \varepsilon_\infty \tag{2}$$

where ε_s, ε_∞ are respectively the static and high frequency values of the permittivity and τ is the dielectric relaxation time. The permittivity is a complex function of frequency and usually is described by its real and imaginary part.

$$\varepsilon_R = \varepsilon_\infty + \frac{\Delta\varepsilon}{1 + \omega^2\tau^2}, \qquad \varepsilon_I = \frac{\Delta\varepsilon\omega\tau}{1 + \omega^2\tau^2} \tag{3}$$

The loss tangent $\tan\delta$ is defined by the ratio of these two parts and characterizes the attenuation of the electromagnetic waves in a medium due to ohmic conductivity σ.

$$\tan\delta_d = \frac{\varepsilon_I}{\varepsilon_R} = \frac{\sigma}{\omega\varepsilon_R} \tag{4}$$

The conductivity σ of the medium is directly proportional to the imaginary part of the dielectric constant.

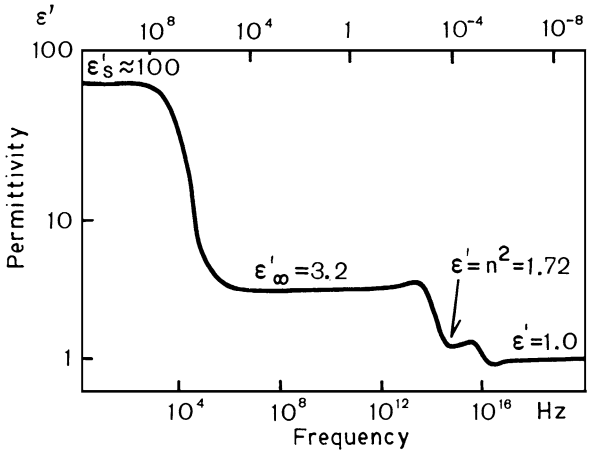

Fig. 5 The real part of the dielectric constant of ice normalised by ε_0 (Fletcher 1970) as function of frequency near $-10°$C

An approximated expression of the attenuation is given by the formula (5)

$$\alpha = 0.129\sqrt{\varepsilon_R} f[\sqrt{(1+\tan^2\delta}-1]^{1/2} \approx 0.091\sqrt{\varepsilon_R} f \tan\delta \approx 0.0009\sigma \text{ dB/m} \quad (5)$$

where σ is in μS m^{-1}. This approximate form of (5) is valid for non-magnetic media with a low loss tangent, such as water ice.

The imaginary part characterizes the attenuation and reaches the maximum at $\omega = \tau^{-1}$.

From (5), one sees that the attenuation coefficient is directly proportional to the frequency. Another way to see this result is that the losses are directly proportional to the conductivity of the medium (5).

The static dielectric constant of a pure ice is very large and anisotropic, and depends on the orientation of the electric field with respect to the crystal's axis (Bogorodsky et al. 1985) changing from about 105 to 90 at 0°C for parallel and perpendicular field. The values increase at $-50°$. The effect of pressure is small and about 1% per kbar for polycrystalline ice (Chan et al. 1965).

The high-frequency (i.e. at typical radar frequencies) dielectric value is constant over a large frequency band, and is close to 3.2 at 0°C and isotropic within at least 0.5% (Johari and Jones 1978). The temperature dependence of ε_∞ is weak and changes about 1% from 0 to $-15°$C and another 1% down to $-75°$C (Johari and Charette 1975; Johari and Jones 1978). Figure 5 shows the behaviour of the real part of the permittivity as function of the frequency.

The temperature dependence of ε_∞ can be modelled as linear (Chyba et al. 1998).

$$\varepsilon_\infty = 3.02 + 6.41 \times 10^{-4} T \quad (6)$$

and $\Delta\varepsilon$ obeys the Curie-Weiss law:

$$\varepsilon_0 = \varepsilon_\infty + A_C/(T - T_C) \quad (7)$$

with T_c ranging from 15 K to 46 K (Johari and Jones 1978; Kawada 1978).

Chyba et al. (1998) fitted and interpolated Johari and Charette (1975) measurements of the imaginary part of the permittivity (for temperature range 248–272 K) with $T_c = 35$ K and obtained $A_C = 3.54 \times 10^4$. Finally the relaxation time is obtained using the Arrhenius function with the activation energy of about 0.58 eV (Humbel et al. 1953; von Hippel et al. 1971):

$$\tau = C \exp\left(\frac{E}{kT}\right) \tag{8}$$

where $C = 5.3 \times 10^{-16}$ and $k = 8.61 \times 10^{-5}$ eV K^{-1}. The pressure effect is to increase the relaxation time of about 10% between 0 and 500 bars, independent on temperature (Ruepp 1973).

Other data were used by Thompson and Squyres (1990) to obtain slightly different formulas that were compared in the paper by Chyba et al. (1998). The results are similar and remain close. For the experiment definition and the estimation of radar capabilities it's enough to use the above formulas. The attenuation of the electromagnetic waves in the ice can be calculated for lower temperatures using the previous equations. However, for very low frequencies below a few kHz the previous formula can greatly underestimate the attenuation (Chyba et al. 1998). But for a future subsurface sounding radars working at frequencies higher than a few MHz the formulas are probably correct.

In general the values of dielectric parameters for pure polycrystalline ice are close to those for single-crystal ice (Bogorodsky et al. 1985).

Because of the low losses expected in pure water ice, the major effect on the absorption of radar waves will in fact depend on the nature and concentration of impurities in the ice. This is of course difficult to evaluate due to uncertainties and lack of knowledge of the physical nature of impurities for icy satellites. For Europan ice this problem was studied by Chyba et al. (1998) and Moore (2000). The latter considered three types of water ice, produced by three basic processes occurring on Earth: meteoric ice formed by atmospheric precipitations, sea ice formed by the freezing of water close to the atmospheric interface, and marine ice forming beneath ice shelves directly from ocean water. Moore (2000) concluded that similar processes are likely to occur on Europa as well, and that the most probable form of ice would be marine ice.

Chyba et al. (1998) studied the electromagnetic properties of a medium resulting from the mixing of different impurities (rock, dust) into an ice matrix. They used a mixing formula (Sihvola and Kong 1988, 1989) to calculate the dielectric constant of the mixture and the properties of lunar materials as a model for the impurities within the Europan ice. This approach requires many assumptions and gives only some estimation of the dielectric constant that can be used in the evaluation of the radar capabilities.

In addition to the Chyba et al. (1998) approach, Moore (2000) was interested in soluble impurities in ice like F^-, Cl^-, NH_4^+, SO_4^{2-} and H^+ ions. In Table 1 (Moore 2000) the attenuation for different types of impurities in ice is shown, based on laboratory measurements, ice temperature modelling for Europa and some scaling from Earth ice measurements. These data are valid for electromagnetic frequencies of a few tens of MHz.

These calculations are not taking into account a possible scattering of the electromagnetic waves by the ice/pore interfaces that can exist in the crust. The scattering effect plays the same role as attenuation and depends strongly on the dimension of cavities, (voids) in the medium compared to the wavelength. The Mie or Rayleigh approaches (see e.g. Ishimaru 1978) can be used to calculate the extinction of the radar signal.

The scattering of radio waves by surface and by volume irregularities is an important factor which one has to take into account to evaluate the penetration of the radar wave, and the ratio of any subsurface echo to surface clutter. These two parameters are essential to predict the radar performance. The scattering depends strongly, as we wrote above, on the radar wavelength and surface parameters of the body under investigation. This frequency dependence of attenuation requires that subsurface sounding radars operate at low-frequency ($<$100 MHz) in order to achieve a deep penetration. The choice of the frequency has an influence on the instrument characteristics, and especially on the size of the antenna. The

Table 1 Radar absorptions for various ice types and temperatures, taken from Moore (2000)

M	Ice type	Impurity content	α	I	II	III	Notes
0	pure ice	nil	0.0045	1.4–2.4	0.5–0.5	0.2–0.3	Glen and Paren (1975)
1	chloride-dominated Europa ice/ocean	3.5 ppt chlorinity ocean	0.016	4–7	2.5–4	1.6–2.8	Marine ice scaled from Earth ocean, $k_{MI} = 7 \times 10^4$
2	rock/ice	1% lunar soil	0.008	5–6	4–4.7	3.6–4.1	Chyba et al. (1998) recalculated
3	rock/ice	10%lunar soil	0.01	8–9	7–8	6–7	Chyba et al. (1998) recalculated
3	sultato-dominated Europa ice/ocean	10 ppt chlorinity ocean	0.037	9–16	6–11	4–7	Kargel (1991); marine ice, $k_{MI} = 7 \times 10^4$
1	chloride-dominated Europa ice/ocean	3.5 ppt chlorinity ocean	0.05	14–24	10–17	7–12	Marine ice scaled from Earth ocean. $k_0 = 3 \times 10^{-3}$
1	rock/ice	50% lunar soil	0.021	30–33	29–32	28–31	Chyba et al. (1998) recalculated
2	depth-dependent Ronne Ice Shelf marine ice	0–400 μM CI linear rise surface to bottom	varies	34–56	24–40	17–28	0–100% Ronne Ice Shelf ion Content
2	sulfate-dominated Europa ice/ocean	10 ppt chlorinity ocean	0.15	36–61	25–44	18–31	Kargel (1991); marine ice, $k_0 = 3 \times 10^{-3}$
2	Ronne Ice Shelf marine ice	400 μM CI (0.025 ppt salinity) ice	0.15	36–61	25–44	18–31	Moore et al. (1994) LF σ from core samples
0	Baltic Sea ice	ice grown in ≈3 ppt sea water	0.85 (at 270 K)	50–85	26–43	16–27	200 MHz radar measurement

Note. Attenuation, α, is in dB/m at 251 K. Columns I, II, and III are computed two-way attenuations, in dB/km, for ice shells with base temperatures of 270, 260, and 250 K, respectively. The range of values for each of these corresponds to surface temperatures of 50 and 100 K. These values are independent of shell thickness since the temperature profile is stretched to the ice thickness. The M column represents the plausibility of the ice type for Europa; 0 is least likely while 3 is more likely, given the present understanding of Europa. The distribution coefficients k_0 and k_{MI} affecting the marine ice models come from laboratory experiments and Ronne Ice Shelf marine ice measurements, respectively

exact choice of the frequency results from a trade-off between science requirements and technical limitations.

Due to the lack of knowledge of physical parameters controlling scattering, it is rather difficult to predict its effects with accuracy. For example, Eluszkiewicz (2004) concluded that the presence of a regolith about 1 km thick with an 1% of cavities whose size is comparable to the radar wavelength will make radar wave penetration impossible.

In spite of all these uncertainties, experience has demonstrated that data such as those presented in Table 1 provide the capability to evaluate the radar performance with sufficient accuracy. At the time in which the MARSIS (Picardi et al. 2004) and SHARAD (Seu et al. 2007a) radar sounding experiments were proposed, radar sounding of planetary bodies was deemed problematic if not impossible, in spite of data obtained by the ALSE experiment on board the Apollo 17 spacecraft (Phillips et al. 1973), but results at Mars (e.g. Picardi et al. 2005; Plaut et al. 2007; Seu et al. 2007b; Mouginot et al. 2009) have conclusively demonstrated that this technique is effective in the investigation of planetary bodies from orbit.

4.2 Radar Performance

The data from Table 1 can be used to evaluate penetration depth in the subsurface of icy bodies. As we want to use the radar to study interiors using the reflection from discontinuities and/or diffraction of signals, the reflection and transmission coefficients are also factors determining how much of the incoming signal amplitude is reflected and transmitted. These quantities allow the estimation of the power of the incoming radar signal and therefore the radar capabilities. The following equations summarize the factors affecting radar performance:

$$P_{Rx} = \frac{P_{Tx}(1-|r_{ice}|^2)\tau_p B G_{Tx} G_{Rx} \lambda^2 r_{layer}^2 10^{-\alpha z} L_{sys}}{(4\pi)^2 (2(R+z))^2} \tag{9}$$

$$SNR = \frac{P_{Rx}}{P_{noise}} = \frac{P_{Tx}(1-|r_{ice}|^2)\tau_p G_{Tx} G_{Rx} \lambda^2 r_{layer}^2 10^{-\alpha z} L_{sys}}{(4\pi)^2 (2(R+z))^2 k T_{ref} N_f} \tag{10}$$

where

P_{Tx} = peak RF power during transmission of the pulse
G_{Tx} = antenna gain on transmission
G_{Rx} = antenna gain on reception
λ = operating wavelength
r_{ice} = effective reflectivity of the ice-atmosphere interface
r_{layer} = effective reflectivity of an internal layer
α = 2-way attenuation through ice of thickness z
L_{sys} = system losses including internal transmission losses and losses within the antenna during transmission
R = range from satellite to ice surface
z = depth from the surface to the internal layer
P_{noise} = $kT_{ref}BN_f$ where
k = Boltzmann constant
T_{ref} = antenna reference temperature
B = bandwidth of transmitted pulse

N_f = system noise figure
τ_p = pulse duration

Modern radars transmit a modulated signal that provides a compression gain so that the effective echo power received within the pulse bandwidth is increased by a factor $\tau_p B$.

This equation is given here only to highlight different factors playing a role in radar detection capabilities. The noise level is one of the factors limiting performance. For low frequency radars (1–50 MHz) the galactic noise temperature varies between 10^7 to 10^4 K. In the Jovian environment its radio noise increases the noise temperature of about 10^{10} to 10^6 K but on the anti-Jovian side of a moon the influence is negligible.

The altitude of the spacecraft also plays an important role. For a radar placed on an orbit at 100 km of altitude, at the frequency of 20 MHz (the SHARAD radar frequency), with the noise temperatures of the order of 5×10^4 K, the antenna gain of 10 dB, the peak power of 100 W and a modulated pulse of 200 μs, the signal to noise ratio is:

$$SNR \approx 130 - \alpha Z + 20 \log r_{layer} + 10 \log(1 - |r_{ice}|^2) + L_{sys} \tag{11}$$

The transmission loss between the air/ice interface is about 1 dB, and the reflection loss at the interface within the ice is estimated to be between -10 to -20 dB. L_{sys} is assumed to be -3 dB.

Finally, as one needs about 20 dB SNR in order to adequately process the signal, the acceptable losses inside the ice are found to be of about 85 dB. Coherent processing can reduce the noise power and then increase the SNR. Typical gains for coherent processing are of the order of 10–20 dB. In this analysis surface clutter effects are not taken into account, but they can easily reduce the signal detection capability by a comparable amount, although they can in turn be reduced through Doppler filtering. This is why the acceptable value for attenuation can still be maintained at 85 dB.

From Table 1 it can be seen that radar penetration inside pure ice can exceed 40 km. The most probable losses, however, are between 6 and 16 dB/km, which will clearly limit the penetration to 5 to 15 km.

5 Laboratory Studies Relevant to Interpretation of Radar Observations

As mentioned above, in order to estimate the maximum penetration depth of a subsurface radar signal in the icy moons crust of the Solar System, the electromagnetic properties of the materials forming the solid and/or liquid layering sequence should be known. Several laboratory techniques can be used to measure the complex permittivity of ice or icy soil simulants: some of them operate in the frequency domain (FD) regime, others in the time domain (TD) regime. The FD techniques (dielectric spectroscopy) allows one to perform a straightforward measurement of both real and imaginary part of the permittivity, in a limited range of frequency (in fact, it is not possible to use just one instrument to measure the permittivity from zero-frequency up to the microwave region). Conversely, to extract the same parameters as a function of frequency, the TD techniques need a transformation from time to frequency domain and a dielectric model to fit the experimental data. However, if no dispersion is observed, time domain analysis can be a very fast and reproducible technique to estimate the dielectric permittivity and the DC conductivity of a material.

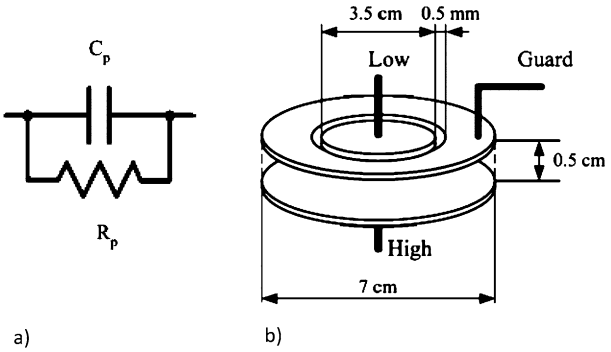

Fig. 6 (**a**) Equivalent circuit; (**b**) Schematic of a capacitance cell to measure electrical properties of granular or liquid materials

5.1 Frequency Domain Measurements

Usually, the laboratory techniques for measuring the electromagnetic properties of granular or liquid materials at hertz-to-megahertz frequencies are based on the equivalent circuit analysis performed through *L*-*C*-*R* meters (Pettinelli et al. 2003). Conductivity and permittivity are obtained by measuring the magnitude and phase of the electrical impedance of a capacitive cell (i.e. Parallel Plate Capacitor—PPC) filled with the material being tested.

With reference to the lumped equivalent circuit shown in Fig. 6a, the current in the cell, can be expressed through its complex admittance Y^*:

$$I = V_g \cdot Y^* = V_g \cdot \left(\frac{1}{R_p} + j\omega C_p \right) \tag{12}$$

Using the geometrical features of the cell the measured values of capacitance C_p and parallel resistance R_p can be related to the real and imaginary parts of the complex permittivity of the material enclosed between the electrodes.

In particular, if A is the surface of the guarded electrode (the plate connected to the "low" terminal in Fig. 6) and d is the spacing between the two parallel plates, one obtains:

$$\varepsilon' = \frac{d}{A} \cdot \frac{C_p}{\varepsilon_0} = \frac{C_p}{C_0}; \qquad \varepsilon'' = \frac{d}{A} \cdot \frac{1}{\omega \varepsilon_0 R_p} = \frac{1}{\omega C_0 R_p} \tag{13}$$

Note that, a precise knowledge of the cell geometry is not strictly required to get accurate measurements, as both the real and imaginary terms of permittivity can be calculated using the previously measured value of the capacitance with the cell empty (i.e. C_0). The effect of the fringing field at the edges of the capacitor plates is cancelled by using a guarded electrode (see Fig. 6).

Several types of capacitive cell can be used to estimate the dielectric parameters of a material; the choice depends on the material itself (soil, ice or mixtures) and the pressure and temperature that should be applied to the sample. As an example, Fig. 7a and b show a parallel plate cell and a coaxial cell suitable for granular or icy samples measured at atmospheric pressure.

The maximum frequency achievable with the capacitor cell technique is of the order of few tens of MHz, therefore suitable to support the investigations of orbiting subsurface radars like MARSIS or SHARAD. However, if a higher frequency range should be investigated (from hundreds of MHz to few GHz), the most common technique used to extract the real and imaginary part of the permittivity is the measurement of the scattering parameters

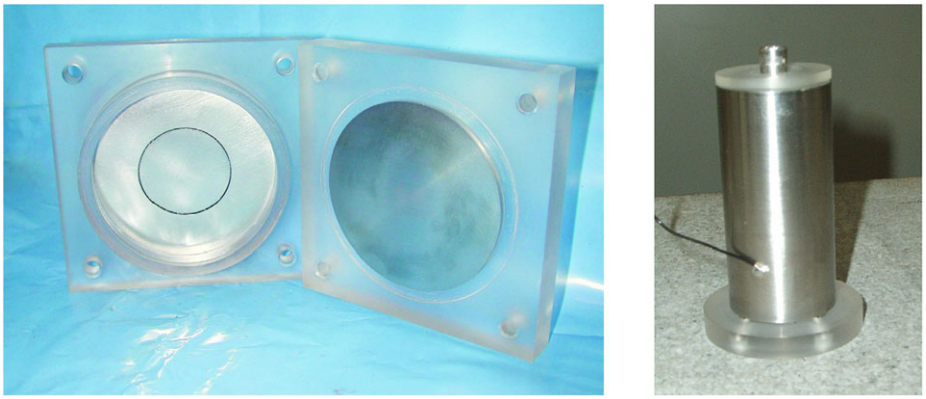

(a) (b)

Fig. 7 (**a**) Parallel plate capacitor cell; (**b**) Coaxial capacitor cell

of a coaxial line, connected to a network analyzer (see for example the review of Stuchly and Stuchly 1980).

5.2 Time Domain Measurements

The use of Time Domain Reflectometry (TDR) technique for permittivity measurements is based on evaluating the velocity of a step-like signal which travels along a transmission line filled with the material under test or embedded in it (for details see Topp and Ferré 2002, and Robinson et al. 2003). The TDR signal has a broad band and the upper frequency, in a sample, can extend up to about 500 MHz.

A basic TDR system consists of a pulse generator, a sampler, an oscilloscope, a coaxial cable, and a transmission line probe (see Fig. 7). The pulse generator applies a fast rise-time voltage step (∼200 ps) to a 50-ohm coaxial cable and triggers a sampler. The step pulse travels down the coaxial cable, until it reaches the probe, where part of the signal is reflected back toward the cable tester due to an impedance mismatch, and part passes along the line in the material itself. The signal traveling in the material ultimately reaches the end of the probe, sending a reflection back toward the oscilloscope.

The waveform displayed on the oscilloscope represents the superposition of incoming and reflected waves (in phase or in counter phase), generated at every impedance mismatch in the system. From the propagation time of the wave front along the probe, the pulse velocity can be calculated according to the following equation:

$$v = \frac{2L}{t} \tag{14}$$

where t is the two-way travel time (from t_2 to t_3 in Fig. 8) and L is the probe length. Assuming that the material is homogeneous within the sample, the electromagnetic wave velocity is given by:

$$v = \frac{c}{\mathrm{Re}\sqrt{\varepsilon^* \mu^*}} \tag{15}$$

where c is the electromagnetic wave velocity in the vacuum (3×10^8 m/s), and ε^* and μ^* are the material complex permittivity and complex magnetic permeability, respectively.

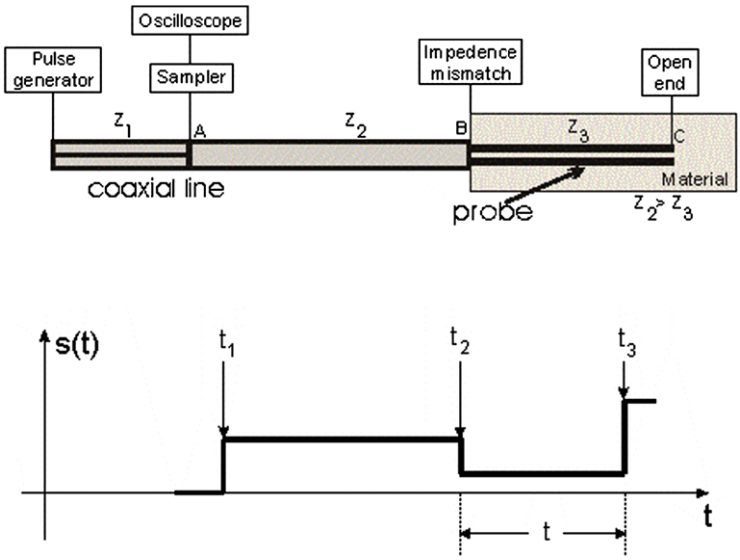

Fig. 8 Schematic of TDR measurement technique

Equation (15) can be expressed in a more explicit form as:

$$v = \frac{c\sqrt{2}}{\sqrt{\mu'\varepsilon' - \mu''\varepsilon'' + |\varepsilon^*||\mu^*|}} \tag{16}$$

If magnetic materials are not present, as in the case of pure ice or icy mixtures, TDR travel-time measurements can be used to estimate the *apparent relative dielectric permittivity*, ε_{ra}, throughout the following

$$\varepsilon_{ra} = \left(\frac{ct}{2L}\right)^2 \tag{17}$$

which takes into account for both real and imaginary parts of the permittivity.

Figure 9a shows a TDR configuration that can be easily used in icy material, where the probe can be directly inserted in the material before freezing, whereas Fig. 9b shows a TDR configuration suitable to measure the dielectric properties of liquids or granular materials.

Furthermore, the analysis in time domain of the TDR wave forms allows one to estimate also the DC conductivity using the equation (Giese and Tiemann 1975):

$$\sigma_{GT} = \sqrt{\frac{\varepsilon_0}{\mu_0}}\frac{1}{L}\left(\frac{Z_0}{Z_c}\right)\left(\frac{2V_0 - V_f}{V_f}\right) \tag{18}$$

where L is the probe length, Z_0 is the probe impedance in air and Z_c is the coaxial cable impedance, V_0 is the input voltage and V_f is the asymptotic voltage value (see Fig. 10). For a detail description of the DC conductivity evaluation with TDR see Robinson et al. (2003).

5.3 Determination of Electromagnetic Parameters via Scatter Function

The TDR wave form carries information on the electromagnetic properties of the sample under test in a wide band of frequency. The frequency response of a TDR device, can be

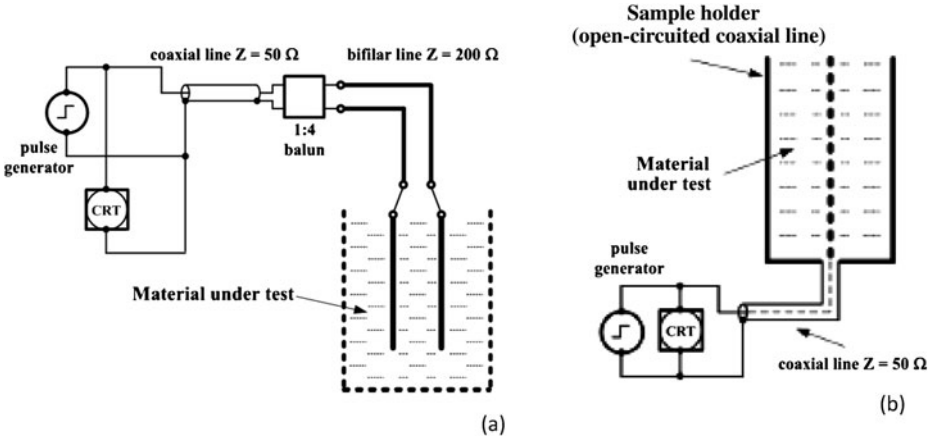

Fig. 9 (**a**) Schematic drawing of a TDR system where the probe consists of two parallel metal rods which are inserted in the material to be tested; (**b**) the same TDR configuration connected to a coaxial probe

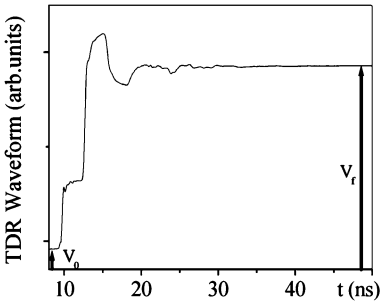

Fig. 10 TDR wave form and relevant parameters used to estimate DC conductivity

conveniently studied by using its transfer function $S(\nu)$. This function allows one to estimate both the material electromagnetic properties and the transmission line parameters, because it can be directly compared with the theoretical expressions.

The theoretical scatter function $S_T(\nu)$ of an open-ended coaxial probe is given by Clarkson et al. (1977), Ramo et al. (1984)

$$S_T(\nu) = \frac{(\rho^* + \exp(-2\gamma L))}{(1 + \rho^* \exp(-2\gamma L))} \tag{19}$$

where L is the probe length, ρ^* is the reflection coefficient

$$\rho^* = \frac{(1 - z\sqrt{(\varepsilon^*(\nu)/\mu^*(\nu))})}{(1 + z\sqrt{(\varepsilon^*(\nu)/\mu^*(\nu))})} \tag{20}$$

and γ is the propagation function

$$\gamma = \frac{j2\pi f}{c}\sqrt{\varepsilon^*(\nu)\mu^*(\nu)} \tag{21}$$

where c is the velocity of light in a vacuum. The quantity z in (20) represents a normalized impedance given by $z = Z_C/Z_P$, where Z_C is the impedance of the cable connecting the

TDR probe to the signal generator and Z_P is the impedance of the TDR probe in air. $\varepsilon^* = \varepsilon' - j\varepsilon''$, $\mu^* = \mu' - j\mu''$ are the e.m. parameters of the test material.

To estimate the probe parameters (Feng et al. 1999; Mattei et al. 2006), calibration measurements in some reference materials (such as water, air, ethanol, etc.) should always be performed. The fitting of the theoretical scatter function $S_T(\nu)$ to the experimental scatter function, allows the evaluation of z and L, since the e.m. properties of the reference materials are known from literature.

Once the probe parameters are known, TDR measurements can be performed in the probe filled with the material under test. The fitting of $S_T(\nu)$ to the experimental scatter function provides the e.m. constitutive parameters. In fact, for non magnetic materials, if the polarization process can be modelled with Debye-like relaxation, the relative complex permittivity is given by

$$\varepsilon^*(\nu) = \varepsilon_\infty + \frac{(\varepsilon_S - \varepsilon_\infty)}{1 + i\,\nu/\nu_{\text{rel}}} + i\,\frac{\sigma_{dc}}{2\pi\,\nu\varepsilon_0} \tag{22}$$

where ε_S is the static value of permittivity, ε_∞ its high frequency limit, ν_{rel} is the relaxation frequency, σ_{dc} is the static conductivity, and ε_0 is the permittivity in a vacuum. $S_T(\nu)$ can be obtained applying (19) and (20), whereas the minimization procedure allows the evaluations of the model parameters and, consequently, the frequency dependence of test material e.m. properties.

6 Laboratory Results on Icy Soil Samples

As examples of the information that can be retrieved from dielectric measurements with FD or TD techniques, we present here some data acquired on CO_2 ice and some icy mixtures. The measurements were performed in the frequency domain (100 Hz–1 MHz) using a capacitive cell (PPC) and in the time domain using a two-prong transmission line. These two techniques are particularly suitable to perform dielectric measurements on icy samples because they offer several advantages: (i) data acquisition is simple and fast; (ii) sample volume is large (i.e. the bulk properties of a material are measured); and (iii) the experimental techniques are reproducible and the results are consistent.

Figure 11a and b show real and imaginary parts of permittivity measured in the same frequency range on two samples prepared with CO_2 ice (ice powder) and CO_2 ice mixed with volcanic sand. For comparison, in the figures the plots for the same dry sand are shown as well. Table 2 summarises volume fractions and density of the materials under test. The data confirm the non-polar behaviour of CO_2 ice, as the real part of the permittivity is very low (about 1.4). The $\varepsilon' \cong 2$ measured for the mixture CO_2 ice and sand is in general agreement with what is reasonably expected. Indeed the dielectric constant of the mixture should exhibit a sort of average between the $\varepsilon' \cong 1.4$ of CO_2 ice and that of the anhydrous sand ($\varepsilon' \cong 3$).

The plot of the imaginary parts of permittivity shows the general tendency of low temperature mixtures to behave like good insulators because the mobility of ions significantly slowed down by the freezing process.

More extended measurements have been conducted on CO_2 ice and icy mixtures with TDR techniques. Table 3 summarises the information on volume fractions and density of the samples and the apparent permittivity values (with the uncertainties) measured with the TD method (for detail see Pettinelli et al. 2003). Note that there are little differences in the apparent permittivity values of the samples presented in the table, with different materials having approximately the same permittivity.

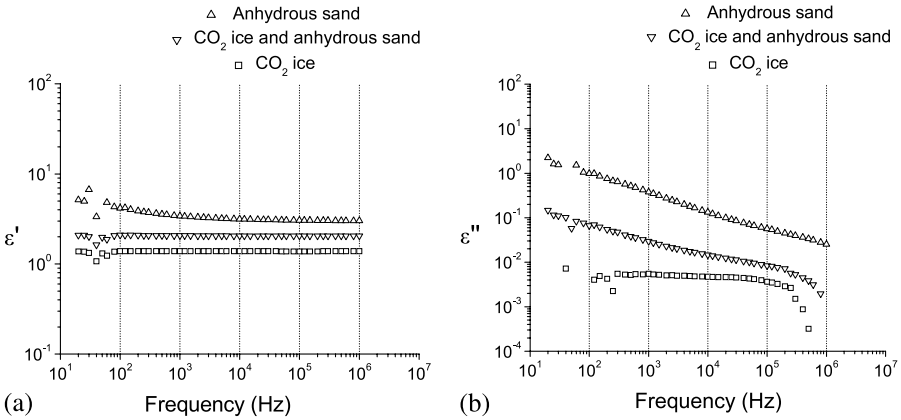

Fig. 11 Real (**a**) and imaginary (**b**) part of permittivity of CO_2 ice and volcanic sand. Comparison with the values measured for anhydrous volcanic sand at room temperature

Table 2 Volume fractions and density of the samples shown in Figs. 11

Material	Volume fractions (%)	Density ($g\,cm^{-3}$)
CO_2 powder (−75°C)	$V_{CO_2} = 70.3\%$ $V_{air} = 29.7\%$	1.05
dry Vulcano sand (24.4°C)	$V_{sand} = 55.9\%$ $V_{air} = 44.1\%$	2.58 (grain density)
CO_2 powder + sand	$V_{sand} = 31.7\%$ $V_{CO_2} = 35.7\%$ $V_{air} = 32.6\%$	–

7 Laboratory Measurements Needed to Support Interpretation of Radar Observations

At the present stage an accurate survey of the literature available, shows a lack of data on dielectric properties of icy materials, gas hydrates (clathrates), and salt doped ice in the frequency range of interest (i.e. tens of MHz or higher) to define the performance properties (the maximum penetration depth) of future subsurface radars capable of investigating the interior structure of the icy moons of the Solar System. The vast majority of dielectric measurements, in fact, have been collected at low frequency (below 1 MHz) (Thompson and Squyres 1990; Lorenz 1998; Chyba et al. 1998; Moore 2000; Pettinelli et al. 2003; Grimm et al. 2008). These data show, in general, that the impurities in the ice have the effect of shifting the relaxation time at higher frequencies, however, never exceeding few tens of kHz. In the MHz range, the ice or the icy mixtures seem to have low values of the real part of the permittivity and small values of the conductivity, behaving like non-polar low-loss materials. Therefore, we should expect a transparent behavior of the icy materials in a broadband of frequencies well above the relaxation frequency.

Nevertheless, the definition of the best radar frequency to use to investigate the internal structure of an icy moon crust should be strongly supported by adequate and extensive

Table 3 Volume fractions, density and apparent permittivity experimental values, measured by TDR technique for various samples of solid CO_2, volcanic sand, and mixtures (Pettinelli et al. 2003)

Material	Volume fraction	Density (g cm^{-3})	$\varepsilon_{ra} \pm \Delta\varepsilon_{ra}$
CO_2 ice	–	1.50	2.12 ±0.04
CO_2 snow	–	–	1.48 ±0.04
CO_2 powder (1)	–	0.99	1.67 ±0.06
CO_2 powder (2)	–	1.01	1.63 ±0.06
CO_2 powder (3)	–	1.02	1.67 ±0.06
dry Vulcano sand	$V_{sand} = 57.5\%$ $V_{air} = 42.5\%$	2.58 (grain density)	3.83 ±0.09
CO_2 snow + glass beads (1)	$V_{glass1} = 37.47\%$ $V_{CO_2} = 62.53\%$	–	2.32 ±0.03
CO_2 snow + glass beads (2)	$V_{glass2} = 20.75\%$ $V_{CO_2} = 79.25\%$	–	1.56 ±0.03
CO_2 powder + sand (1)	$V_{sand1} = 38.2\%$ $V_{CO_2} = 23.8\%$ $V_{air} = 38.0\%$	–	2.6 ±0.2
CO_2 powder + sand (2)	$V_{sand2} = 25.5\%$ $V_{CO_2} = 38.6\%$ $V_{air} = 35.9\%$	–	2.28 ±0.07

laboratory investigations on a sufficient number of composite ice samples. In particular, because the temperature, the impurities, and the density of the icy materials are the parameters that affect the most the dielectric behavior of the simulants, these measurements should be performed systematically changing these two parameters. These types of measurements, however, require a certain level of accuracy: in fact, as shown in Table 3, the permittivity values obtained in the MHz range for different icy soil, might be very close to each other, and in order to distinguish between different materials a small uncertainty should be associated to the measurement. This ambiguity in the dielectric properties also affects strongly the possibility to perform some data inversion and extract some information on the dielectric properties of the deeper layers, like an ocean under an icy crust. Moreover, laboratory measurements can be used to validate a dielectric model. As an example, Table 4 compares, the apparent permittivity values obtained using TDR technique with those calculated using different dielectric models (for detail see Pettinelli et al. 2003).

Among the models presented in Table 4 to predict the average dielectric properties of a mixture, the Tinga model is the most flexible and therefore it was applied to simulate the dielectric behavior of almost all measured mixtures. The results for mixtures of glass beads and air or water are in excellent agreement with experimental data, due to the fact that this model is particularly well suited to describe the dielectric properties of a mixture consisting of a uniform known host material with homogeneous, equally-sized spherical inclusions. Note that, also Rayleigh mixing formula is suitable to estimate the real part of the permittivity of a material on the basis of its density, if the permittivity value of the solid phase is known. However, many other dielectric mixing formulas are present in the literature (see Sihvola 2000), and in order to assess the prediction capability of such models for the icy mixtures, an extensive study combining laboratory-measured and theoretical permittivity values should be performed

Table 4 Comparison between TDR experimental apparent permittivity values and calculated values from models

Material	$\varepsilon_{ra} \pm \Delta\varepsilon_{ra}$	Model		
		Rayleigh 1892	Tinga et al. 1973	Topp et al. 1980
dry glass beads	3.19 ± 0.08	–	3.0	3.3
saturated glass beads (r.t.)	30.0 ± 0.2	–	30.6	29.6
drained glass beads (r.t.)	4.09 ± 0.08	–	–	5.3
CO_2 powder (1)	1.67 ± 0.06	1.6	1.6	–
CO_2 powder (2)	1.63 ± 0.06	1.7	1.7	–
CO_2 powder (3)	1.67 ± 0.06	1.7	1.7	–
dry Vulcano sand	3.83 ± 0.09	–	3.9	3.0
CO_2 snow + glass beads (1)	2.32 ± 0.03	–	2.7	–
CO_2 snow + glass beads (2)	1.56 ± 0.03	–	1.5	–
CO_2 powder + sand (1)	2.6 ± 0.2	–	3.6	–
CO_2 powder + sand (2)	2.28 ± 0.07	–	2.8	–

Vulcano sand: $\varepsilon_{grain} \cong 17$ (calculated with Rayleigh mixing formula)
Glass beads: $\varepsilon_{grain} = 7.2$

Finally, laboratory measurements are fundamental to help calculate the total attenuation coefficient (ohmic + volumetric scattering) for an electromagnetic wave propagating through an inhomogeneous medium. Tables 5a and b show the total attenuation and the maximum penetration depth of a 225 MHz radar signal in different icy media with basaltic inclusions (for detail see Pettinelli et al. 2007). Again in this case, both dielectric and magnetic properties of the materials forming the mixtures and the inclusions have been measured using the above described FD techniques.

8 Summary and Recommendations

In this chapter, we discussed the application of subsurface radar sounding from orbit to the study of icy moons. We first summarized known radar properties of icy moon surfaces, and discussed existing subsurface radar observations of other planetary bodies. We then presented the main physical parameters of a planetary crust affecting the performance of a radar sounder, concluding that in icy moons a radar sounder should be able to detect dielectric discontinuities at depths of several kilometers to a few tens of kilometers, depending on the nature of the materials through which the electromagnetic pulse propagates. We finally reviewed methods and results for the measurements of dielectric properties of natural materials affecting radar performance, providing suggestions for laboratory activities in support of future subsurface radar observations of icy moons.

Subsurface radar sounding is the only existing remote sensing technique for the study of planetary subsurfaces. Radar sounders have been successfully flown to the Moon and are currently operating at Mars, while another instrument of this kind is on its way to a comet nucleus. Radar experiments are being considered for future missions to near-Earth asteroids, to Vesta and to the icy moons of giant planets. In spite of this, the body of knowledge associated with this technique is still relatively small compared to other remote sensing methods such as spectroscopy, and notions on the correct use and interpretation of data are not yet widespread in the planetary community.

Table 5 Maximum penetration depth at which an interface can be detected below an icy soil with 10% volume fraction of basaltic inclusions (a) and 20% volume fraction of basaltic inclusions (b)

a (10% volume fraction)			
Scenarios	225 MHz		
	Radius of the inclusions (mm)	α_{tot} (dB/m)	L (m)
CO_2/Basalt	200	0.13	43
CO_2&DrySoil/Basalt	200	0.11	40
IcySoil/Basalt	200	0.082	22
b (20% volume fraction)			
Scenarios	225 MHz		
	Radius of the inclusions (mm)	α_{tot} (dB/m)	L (m)
CO_2/Basalt	200	0.49	21
CO_2&DrySoil/Basalt	200	0.42	21
IcySoil/Basalt	200	0.084	27

We are convinced that radar sounding has the potential to provide an enormous increase in our knowledge of the geology of planetary bodies, because of its unique capability to explore the third dimension and its yet limited application to planetary exploration. Because of the transparency of ice-rich materials to low-frequency electromagnetic waves, we strongly advocate the use of this technique in the study of icy bodies in the Solar System. We also deem that more work is required to fully utilize radar sounding data for the quantitative determination of subsurface properties, an inverse problem of no small complexity. Laboratory measurements of the dielectric parameters of natural materials occurring on planetary bodies are a key activity towards this end.

References

J.E. Baron, G.L. Tyler, R.A. Simpson, Icarus **164**, 404–417 (2003)
G.J. Black, D.B. Campbell, L.M. Carter, Icarus **191**, 702–711 (2007)
D.D. Blankenship, D.A. Young, W.B. Moore, J.C. Moore, in *EUROPA*, ed. by R.T. Pappalardo, W.B. McKinnon, K. Khurana (The University of Arizona Press, Tucson, 2010), pp. 631–653
V. Bogorodsky, C. Bentley, P. Gudmandsen, *Radioglaciology* (Reidel, Dordrecht, 1985). ISBN 90-277-1893-8
R.K. Chan, D.W. Davidson, E. Whalley, J. Chem. Phys. **43**, 2376–2383 (1965)
C.F. Chyba, S.J. Ostro, B.C. Edwards, Icarus **134**, 292–302 (1998)
T.S. Clarkson, L. Glasser, R.W. Tuxworth, G. Williams, Adv. Mol. Relax. Proc. **10**, 173–202 (1977)
V.R. Eshleman, Science **234**, 587–590 (1986)
J. Eluszkiewicz, Icarus **170**, 234–236 (2004)
N.H. Fletcher, *The Chemical Physics of Ice* (Cambridge University Press, New York, 1970)
W. Feng, C.P. Lin, R.J. Dechamps, V.P. Drnevich, Water Resour. Res. **35**, 2321–2331 (1999)
K. Giese, R. Tiemann, Adv. Mol. Relax. Proc. **7**, 45–59 (1975)
J.W. Glen, J.G. Paren, J. Glaciol. **15**, 15–37 (1975)
R.E. Grimm, D.E. Stillman, S.F. Dec, M.A. Bullock, J. Phys. Chem. B **112**, 15382–15390 (2008)
T. Hagfors, I. Dahlstrom, T. Gold, S.-E. Hamran, R. Hansen, Icarus **130**, 313–322 (1997)
B. Hapke, Icarus **88**, 407–417 (1990)
F. Humbel, F. Jona, P. Scherrer, Helv. Phys. Acta **26**, 17–32 (1953)

Y.A. Ilyushin, V.E. Kunitsyn, J. Commun. Technol. Electron. **49**, 154–165 (2004)
A. Ishimaru, *Wave Propagation and Scattering in Random Media* (Academic Press, New York, 1978)
G.P. Johari, P. Charette, J. Glaciol. **14**, 293–303 (1975)
G.P. Johari, S.J. Jones, J. Glaciol. **21**, 259–276 (1978)
J.S. Kargel, Icarus **94**, 368–390 (1991)
S. Kawada, J. Phys. Soc. Jpn. **44**, 1881–1886 (1978)
W. Kofman et al., Adv. Space. Res. **21**(11), 1589–1598 (1998)
W. Kofman, A. Herique, J.-P. Goutail, T. Hagfors, I.P. Williams, E. Nielsen, J.-P. Barriot, Y. Barbin, C. Elachi, P. Edenhofer, A.-C. Levasseur-Regourd, D. Plettemeier, G. Picardi, R. Seu, V. Svedhem, Space Sci. Rev. **128**(1–4), 413–432 (2007)
J.-P. Lebreton et al., in *Lunar and Planetary Institute Science Conference Abstracts*, vol. 40 (2009), p. 2383
R.D. Lorenz, Icarus **136**(2), 344–348 (1998)
E. Mattei, A. Di Matteo, A. De Santis, G. Vannaroni, E. Pettinelli, Water Resour. Res. **42** (2006). doi: 10.1029/2005WR004728
J.C. Moore, Icarus **147**, 292–300 (2000)
J.C. Moore, A.P. Reid, J. Kipfstuhl, J. Geophys. Res., Oceans **99**(C3), 5171–5180 (1994)
J. Mouginot, W. Kofman, A. Safaeinili, C. Grima, A. Herique, J.J. Plaut, Icarus **201**(2), 454–459 (2009)
J. Mouginot, W. Kofman, A. Safaeinili, A. Herique, Planet. Space Sci. **56**, 917–926 (2008)
J.-F. Nouvel, A. Herique, W. Kofman, A. Safaeinili, Radio Sci. **39**(2004), 1013 (2004)
T. Ono, A. Kumamoto, H. Nakagawa, Y. Yamaguchi, S. Oshigami, A. Yamaji, T. Kobayashi, Y. Kasahara, H. Oya, Science **323**, 909–912 (2009)
S.J. Ostro, D.B. Campbell, R.A. Simpson, R.S. Hudson, J.F. Chandler, K.D. Rosema, I.I. Shapiro, E.M. Standish, R. Winkler, D.K. Yeomans, R. Velez, R.M. Goldstein, J. Geophys. Res. **97**, 18227–18244 (1992)
S.J. Ostro et al., Icarus **183**, 479–490 (2006)
E. Pettinelli, G. Vannaroni, A. Cereti, F. Paolucci, G. Della Monica, M. Storini, F. Bella, J. Geophys. Res., Planets **108**(E4), 8029–8040 (2003)
E. Pettinelli, P. Burghignoli, A. Galli, A.R. Pisani, F. Ticconi, G. Vannaroni, F. Bella, in *IEEE-TGRS 2007*, vol. 48 (2007), pp. 1271–1281
R.J. Phillips et al., NASA Spec. Publ. **330**(22), 1–26 (1973)
R.J. Phillips et al., Science **320**, 1182–1185 (2008)
G. Picardi et al., in *Mars Express: The Scientific Payload*, ed. by A. Wilson, A. Chicarro vol. SP-1240 (ESA, Noordwijk, 2004), pp. 51–69
G. Picardi et al., Science **310**, 1925–1928 (2005)
G. Picardi et al., in *Radar Conference, RADAR'08*, IEEE, 26–30 May 2008 (2008), pp. 1–5
J.J. Plaut et al., Science **316**, 92–95 (2007)
S. Ramo, J.R. Whinnery, T.V. Duzer, *Fields and Waves in Communication Electronics* (Wiley, New York, 1984)
Lord Rayleigh J.W. Strutt, Philos. Mag. **4**, 481–502 (1892)
D.A. Robinson, S.B. Jones, J.M. Wraith, D. Or, R.P. Fredman, Vadose Zone J. **2**, 444–475 (2003)
R. Ruepp, in *Physics and Chemistry of Ice*, ed. by E. Whalley, S.J. Jones, L.W. Gold (R. Soc. Can., Ottawa, 1973), pp. 179–186
F. Russo, M. Cutigni, R. Orosei, C. Taddei, R. Seu, D. Biccari, E. Giacomoni, O. Fuga, E. Flamini, in *Radar Conference, RADAR'08*, IEEE, 26–30 May 2008 (2008), pp. 1–4
A. Safaeinili, W. Kofman, J.-F. Nouvel, A. Herique, R.L. Jordan, Planet. Space Sci. **51**, 505–515 (2003)
D.E. Smith et al., J. Geophys. Res. **106**, 23 689–23 722 (2001)
R. Seu, R.J. Phillips, D. Biccari, R. Orosei, A. Masdea, G. Picardi, A. Safaeinili, B.A. Campbell, J.J. Plaut, L. Marinangeli, S.E. Smrekar, D.C. Nunes, J. Geophys. Res. **112**, E05S05 (2007a)
R. Seu et al., Science **317**, 1715–1718 (2007b)
M.A. Stuchly, S.S. Stuchly, IEEE Trans. Instrum. Measur. **29**(3) (1980)
A.H. Sihvola, Subsurf. Sens. Technol. Appl. **1**, 393–415 (2000)
A.H. Sihvola, J.A. Kong, IEEE Trans. Geosci. Remote Sens. **26**, 420–429 (1988)
A.H. Sihvola, J.A. Kong, IEEE Trans. Geosci. Remote Sens. **27**, 101–102 (1989)
W.R. Thompson, S.W. Squyres, Icarus **86**, 336–354 (1990)
W.R. Tinga, W.A.G. Voss, D.F. Blossey, J. Appl. Phys. **44**, 3897–3902 (1973)
G.C. Topp, P.A. Ferré, in *Methods of Soil Analysis: Part 4, Physical Methods*, ed. by J.H. Dane, G.C. Topp, Soil Sci. Soc. Am. Book Ser, vol. 5 (Springer, Berlin, 2002), pp. 417–421
G.C. Topp, J.L. Davis, A.P. Annan, Water Resour. Res. **16**(3), 574–582 (1980)
P. Zarka, B. Cecconi, W.S. Kurth, J. Geophys. Res. (Space Phys.) **109**, 9 (2004)
Z. Zhang, E. Nielsen, J.J. Plaut, R. Orosei, G. Picardi, Planet. Space Sci. **57**, 393–403 (2009)
A. von Hippel, D.B. Knoll, W.B. Westphal, J. Chem. Phys. **54**, 134–134 (1971)